

Electron and hole polaron accumulation in low-bandgap ambipolar donor-acceptor polymer transistors imaged by infrared microscopy

O. Khatib,^{*} A. S. Mueller, and H. T. Stinson*Department of Physics, University of California, San Diego, La Jolla, California 92093, USA*

J. D. Yuen

Physics Department and Alan G. MacDiarmid Nanotech Institute, University of Texas at Dallas, Richardson, Texas 75080, USA

A. J. Heeger

Center for Polymers and Organic Solids, University of California, Santa Barbara, California 93106, USA

D. N. Basov

Department of Physics, University of California, San Diego, La Jolla, California 92093, USA

(Received 24 July 2014; revised manuscript received 19 November 2014; published 8 December 2014)

A resurgence in the use of the donor-acceptor approach in synthesizing conjugated polymers has resulted in a family of high-mobility ambipolar systems with exceptionally narrow energy bandgaps below 1 eV. The ability to transport both electrons and holes is critical for device applications such as organic light-emitting diodes and transistors. Infrared spectroscopy offers direct access to the low-energy excitations associated with injected charge carriers. Here we use a diffraction-limited IR microscope to probe the spectroscopic signatures of electron and hole injection in the conduction channel of an organic field-effect transistor based on an ambipolar DA polymer polydiketopyrrolopyrrole-benzobisthiadiazole. We observe distinct polaronic absorptions for both electrons and holes and spatially map the carrier distribution from the source to drain electrodes for both unipolar and ambipolar biasing regimes. For ambipolar device configurations, we observe the spatial evolution of hole-induced to electron-induced polaron absorptions throughout the transport path. Our work provides a platform for combined transport and infrared studies of organic semiconductors on micron length scales relevant to functional devices.

DOI: [10.1103/PhysRevB.90.235307](https://doi.org/10.1103/PhysRevB.90.235307)

PACS number(s): 78.30.Jw, 72.80.Le, 85.30.Pq, 85.30.Tv

I. INTRODUCTION

Organic semiconductors continue to evolve as a viable and attractive alternative to conventional silicon-based electronics [1]. Much effort is being devoted to reducing and tuning energy bandgaps between the highest occupied molecular orbital (HOMO) and the lowest unoccupied molecular orbital (LUMO) levels in π -conjugated polymers to improve performance [2–4]. Specifically, the donor-acceptor (DA) approach to synthesizing polymers has led to a new generation of high-mobility ambipolar systems, a necessary precondition for many transistor, photovoltaic, and light-emitting device applications [5–8]. Recently, DA polymers based on acceptor benzobisthiadiazole (BBT) [7,9,10] and donor diketopyrrolopyrrole (DPP) [10–15] have demonstrated strong ambipolarity as well as exceptionally low optical energy bandgaps as small as 0.5 eV [11]. The highest field-effect mobilities in these systems have surpassed $1 \text{ cm}^2 \text{ V}^{-1} \text{ s}^{-1}$ for both electrons and holes [5,11]. Despite much recent progress, however, there remains an incomplete understanding of the fundamental nature of charge transport and dynamics, especially in DA systems that accommodate both types of carriers.

Infrared and optical spectroscopy is a valuable tool for probing the fundamental charged excitations in conducting polymers [16,17]. Spectroscopic probes have direct access

to microscopic details of the electronic states without interference from extrinsic effects that often complicate electrical measurements of field-effect devices, such as contact resistance [1,18]. The electronic structure of these quasi-one-dimensional systems is significantly modified by the presence of additional charges, giving rise to localized states in the forbidden energy gap. The optical transitions to these subbandgap states characterize the nature of the mobile charge carriers in organic semiconductors. Indeed, polaronic absorption in polymers is very well established [16,17,19–23]. However, very few studies thus far have explored spectroscopically both electron and hole polarons in the same system, made possible by the emergence of ambipolar DA polymers. In recent work on homopolymer polyselenophene [24] using charge-modulation spectroscopy (CMS), Chen *et al.* studied the origin of the different transport characteristics of electrons and holes in a semicrystalline ambipolar polymer. Similar charge-induced absorptions, in the near-IR just below the bandgap, were observed for both types of carriers [24]. Such extensive studies for ambipolar copolymer systems, where the choice of donor and acceptor molecules can lead to widely varying electron/hole properties, are still lacking.

Previously, we investigated the infrared response of a new generation of small-bandgap DA copolymers [25] based on BBT. In this work, we expand on these studies with a high-mobility narrow-gap DA system polydiketopyrrolopyrrole-benzobisthiadiazole (PDPPBBT). Using infrared spectroscopy, we observe distinct electronic absorptions for electron and hole polarons accumulated in electrostatically

^{*}okhatib@physics.ucsd.edu

doped PDPPBBT. Further, using a diffraction-limited IR microscope, we register the evolution of the dynamic IR response along the conduction channel during device operation. In conjunction with IR measurements, we measure organic field-effect transistor (OFET) transport *in situ*. We are thus able to directly link macroscopic transistor behavior to the microspectroscopic signatures of electrons and holes in the polymer. Based on the peak position and strength of the IR absorptions, we are able to image the charge density throughout the transistor channel. We create a spatial map of the carrier distribution for several biasing configurations spanning unipolar electron and hole operation, as well as ambipolar device regimes, where both electrons and holes coexist in the transport path. The coexistence of electrons and holes in a single polymer layer forms the basis for emission in devices such as organic light-emitting diodes (OLEDs) and transistors (OLETs). Diffraction-limited IR microscopy offers access to spatial and energy scales characteristic of the electronic excitations responsible for charge transport in functional materials. Our experimental approach sets the stage for combined transport/optics studies of the low-energy physics of polymers and molecular crystals on micron length scales important to practical devices.

II. EXPERIMENTAL DETAILS

PDPPBBT [Fig. 1(a)] was synthesized via Suzuki coupling between the donor (DPP) and acceptor (BBT) moieties following a well-established procedure [9,11]. Thin polymer films were spin coated onto IR-transparent 20–30 Ω cm *n*-doped Si wafers, serving as the back gate, with a 300-nm SiO₂ ($\epsilon = 3.9$) gate insulator. Electrodes were patterned using standard photolithography and were formed with *e*-beam evaporation of 3 nm of nickel followed by 47 nm of gold. Substrate surfaces were passivated with decyltrichlorosilane (DTS) before polymer deposition to lower the density of interfacial trap states.

Source and drain contacts were patterned in an interdigitated device structure with a channel width of 17 μm and length of 200 μm , allowing for spectroscopic monitoring of the gate-induced changes in the IR transmission/reflection on diffraction-limited length scales (detailed below). Transistor measurements and electrical characterization of devices were obtained with dual Keithley 2400 Sourcemeters.

Figure 1(b) shows a schematic of the experimental setup. Infrared spectra were acquired using a diffraction-limited IR microscope (Bruker LUMOS). Broadband light from a SiC Globar source is focused onto the sample surface using an 8 \times Schwarzschild objective. In reflection mode, the return path of the reflected IR beam is along the other half of the objective, while transmission mode uses a bottom illumination configuration [Fig. 1(b)]. The transmitted/reflected IR light is then focused onto a small-area ($d = 100 \mu\text{m}$), midband (650–6500 cm^{-1}) HgCdTe (MCT) detector. In all measurements, we observe similar behavior in IR transmission and reflectance; however, in this work we only report transmission data.

The minimum beam size is determined by an optically transparent, IR opaque software-controlled motorized knife-edge aperture. For electrostatic IR measurements ($V_{DS} = 0$ V), data were recorded with a spectral resolution of 8 cm^{-1}

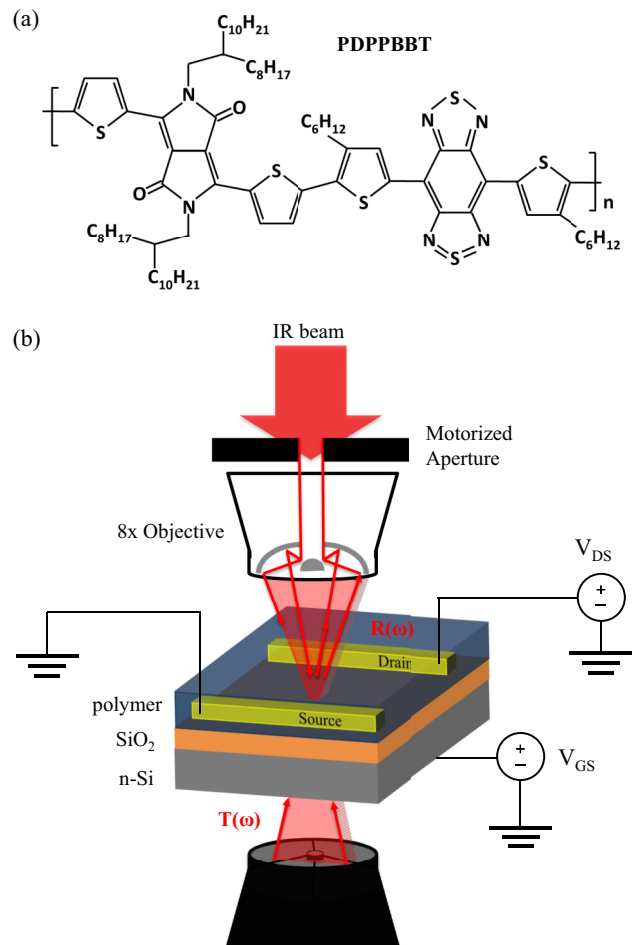


FIG. 1. (Color online) (a) Chemical structure of PDPPBBT. (b) Experimental setup allowing for electrical transport measurements and IR microspectroscopy along the conduction channel between the source and drain electrodes. Small arrows denote the optical path of the IR beam in both reflection (top-illumination) and transmission (bottom-illumination) modes.

and a beam width spanning the distance between the source and drain electrodes (200 μm). For microscopy, the beam size and spectral resolution were reduced to 20 μm and 16 cm^{-1} , respectively. The motorized stage was translated in increments of 20 μm between the source and drain to map out the microscopic IR response during device operation.

To observe gate-induced effects in OFETs, we adapted an Oxford microcryostat (MicrostatHe2) to fit the microscope stage, allowing us to perform repeated IR and transport measurements in high vacuum and low temperature if desired. This was necessary to minimize carrier trapping in the devices, especially for electron transport as we detail below, and achieve a high signal-to-noise ratio. All data reported here were obtained at a pressure of 10^{-6} mbar and at room temperature. The cryostat was fitted with 1.5-mm thick IR-transparent KBr windows and Manganin wires for electrical connections. The entire microscope was encapsulated in a nitrogen purge box.

We note here that introduction of thick windows into the optical path of the microscope shifts the focus of the IR beam. Since the index of refraction of KBr is spectrally flat from the mid-IR through the visible energy range, we do not

expect a discrepancy between the IR and visible focus. For transmission measurements (bottom illumination) we adjusted the microscope condenser to account for both the KBr window and thick Si substrate. Our ability to resolve spectral shifts on 20 μm length scales affirms the validity of our adjustments.

Broadband transmission and absorption spectra were acquired using a Bruker Vertex v70 Fourier transform IR (FTIR) spectrometer. A liquid-helium-cooled Si bolometer, MCT, and InSb detector were used for far-, mid-, and near-infrared measurements, respectively. Broadband IR measurements were performed utilizing a high-vacuum cryostat (Janis Research Company) modified to fit inside a 4x beam condenser (Pike Technologies). The cryostat was equipped with thin (80 μm) polypropylene windows to ensure maximum transparency throughout the entire IR-visible frequency range with minimal absorptions.

III. RESULTS AND DISCUSSION

A. Transport

Figure 2 shows the *in situ* output characteristics of the PDPPBBT OFET prepared for IR microscopy. We observe typical ambipolar transport behavior [26,27]: diodelike evolution of the drain current at low to moderate gate voltages and strong electron or hole saturation currents at higher gate bias. Charge carrier mobilities were calculated in the saturation regime during unipolar operation via the standard equation [1] $I_{DS} = \frac{1}{2} \frac{W}{L} \mu C_i (V_{GS} - V_T)^2$, with mobility determined from $\partial |I_{GS}|^{1/2} / \partial V_{GS}$.

For the device characteristics shown in Fig. 2, the extracted room-temperature electron and hole mobilities were $\mu_e = 0.04 \text{ cm}^2 \text{ V}^{-1} \text{ s}^{-1}$ and $\mu_h = 0.02 \text{ cm}^2 \text{ V}^{-1} \text{ s}^{-1}$, respectively. Electron transport comparable to or stronger than holes is often seen in the DPP family of copolymers [11], consistent with our extracted values. However, these values are quite low compared to typical DPP-based OFETs, which often have electron and hole mobilities surpassing $1 \text{ cm}^2 \text{ V}^{-1} \text{ s}^{-1}$ [5,12–15]. We attribute the low field-effect mobility of the

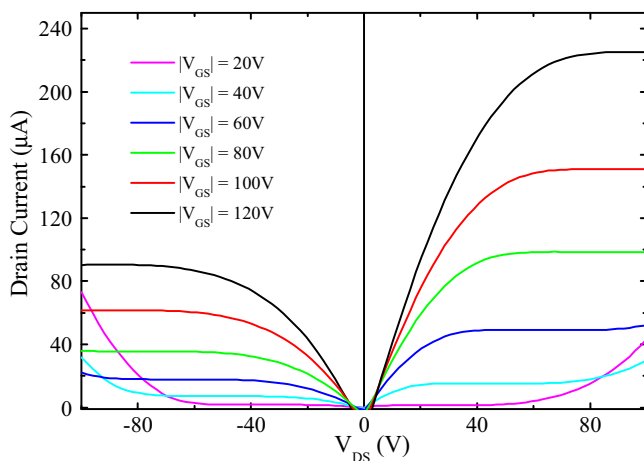


FIG. 2. (Color online) *In situ* I - V characteristics for a SiO_2 -based PDPPBBT device mounted in an IR microscope. Electron and hole mobilities of $\mu_e = 0.04 \text{ cm}^2 \text{ V}^{-1} \text{ s}^{-1}$ and $\mu_h = 0.02 \text{ cm}^2 \text{ V}^{-1} \text{ s}^{-1}$, respectively, were extracted from the saturation regime during unipolar FET operation.

device studied here to a very high density of charge traps at the oxide interface, typically the result of exposure to ambient air and water moisture. The finite time required to mount and wire the sample in the microcryostat (roughly 30 min) in a quasipurged environment ensures a small amount of inevitable exposure to ambient air, leading to a higher trap density.

We found severe carrier trapping for both electron and hole injection, indicative of bias stress: the trapping of injected charges, likely to occur at the semiconductor/dielectric interface [28–30]. Bias stress results in many trapped charges screening the applied electric field and a subsequent shift in the threshold voltage as a function of time [24]. The manifestation of trapping in the IR measurements, where repeated voltage applications are necessary, is discussed later. We were able to mitigate spurious effects of charge trapping by reversing the applied bias between measurements. This was confirmed by remeasuring I - V characteristics and monitoring the leakage current. We emphasize the importance of maintaining a very low pressure environment (10^{-6} mbar in our experiments) by using a cryostat to minimize the role of trapping.

B. Infrared spectroscopy (electrostatic charge injection)

Figure 3 shows the field-induced changes in IR transmission for a PDPPBBT OFET. Data are plotted as negative differential

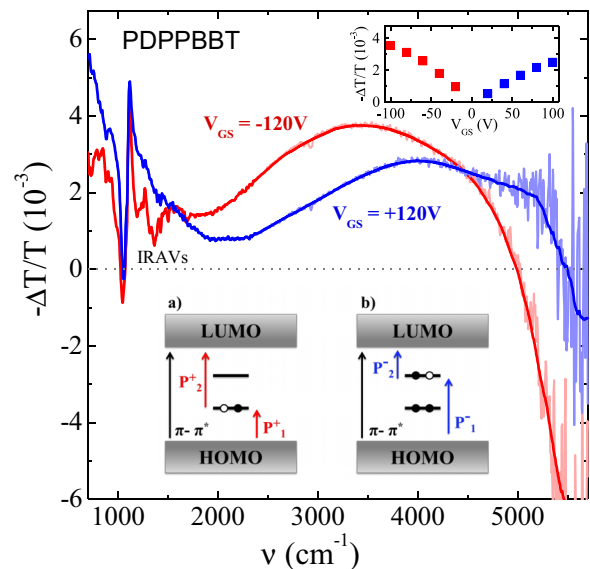


FIG. 3. (Color online) Differential transmission spectra $\Delta T/T$ for PDPPBBT OFET. Red (blue) curves denote the field-induced absorption from a uniform accumulation of a high density of hole (electron) polarons in the conduction channel. The sharp peaks in the 900–1600 cm^{-1} range are infrared-active vibrational modes (IRAVs). The solid lines at higher energies represent averaged curves overlying raw experimental data. The top inset shows the strength of peak absorption ($\omega_h = 3413 \text{ cm}^{-1}$, $\omega_e = 3981 \text{ cm}^{-1}$) as a function of gate voltage V_{GS} . The bottom inset shows a schematic of allowed optical transitions for a single (a) hole and (b) electron polaron state, as well as the neutral π - π^* absorption between the HOMO and LUMO. Based on the peak energies in the experimental data, we ascribe the associated hole and electron absorption bands to the P_2^+ and P_1^- transitions, respectively.

spectra (i.e., absorption):

$$-\frac{\Delta T(\nu)}{T(\nu)} = 1 - \frac{T(V_{GS})}{T(V_{GS} = 0 \text{ V})}, \quad (1)$$

where $T(\nu)$ is the absolute IR transmission. The color scheme adopted previously [25] and used throughout this paper labels positively charged (hole) excitations with red curves and negatively charged (electron) excitations with blue curves. In this electrostatic configuration, the source-drain bias is zero, resulting in a large uniform spatial distribution of holes (electrons) in the channel for $V_{GS} < (>) 0$ V.

At high gate voltages, we find strongly resonant IR absorptions associated with both injected electrons ($V_{GS} = +120$ V) and holes ($V_{GS} = -120$ V). At low energies, an absorption tail extends to just below 2000 cm^{-1} , with several sharp peaks superimposed. In the range $2000\text{--}5500 \text{ cm}^{-1}$, we observe very broad absorption bands, while at higher energies the absorption drops below zero (indicating a significant increase in IR transmission).

The low-energy gate-induced increase in absorption is understood to be dominated by the free-carrier response in the Si substrate, while the large feature at 1100 cm^{-1} is attributed to the SiO_2 oxide layer [22,23]. The smaller peaks superimposed on the substrate absorption, however, are infrared-active vibrational modes (IRAVs). These are symmetric Raman modes in the polymer made IR active by coupling to injected charges [22,31–33]. IRAVs are most evident in the absorption spectra for the hole-doped polymer (red curve in Fig. 3) where the substrate interference is minimal but are otherwise too difficult to discriminate from the background and are only briefly discussed.

The broad absorption bands from 2000 cm^{-1} are attributable to polarons: a result of adding free carriers to a neutral polymer chain. Polarons are formed when injected charge carriers distort the local bond arrangement of the polymer backbone, creating an energy well and resulting in self-localization. These energy minima create bound states in the bandgap, leading to the characteristic subgap absorption features. The bottom inset in Fig. 3 shows a schematic of the optical transitions for a single positive [Fig. 3(a)] or negative [Fig. 3(b)] charge added to a polymer chain, as well as the neutral HOMO-LUMO transition. The difference in energy between the polaronic states and the HOMO and LUMO orbitals indicates the energy gained by the system from the geometrical relaxation associated with the lattice distortion [19,34,35].

IRAV and polaron spectral features are a hallmark of conducting polymers and are very well understood in the context of both electrochemical and electrostatic doping [7,10,19,34–39]. The decrease of the gate-induced change in absorption below zero at energies just above the polaronic response is indicative of polymer bleaching. Indeed, the population of charged molecules increases with doping at the expense of the neutral $\pi\text{-}\pi^*$ absorption (bottom inset in Fig. 3) that defines the optical energy gap.

To closely examine the gate-induced modification of PDPPBBT near the polymer absorption edge, in Fig. 4 we show similarly obtained differential transmission spectra for a separate device recorded in a broadband FTIR spectrometer. Gate-induced absorption spectra (blue and red curves) are

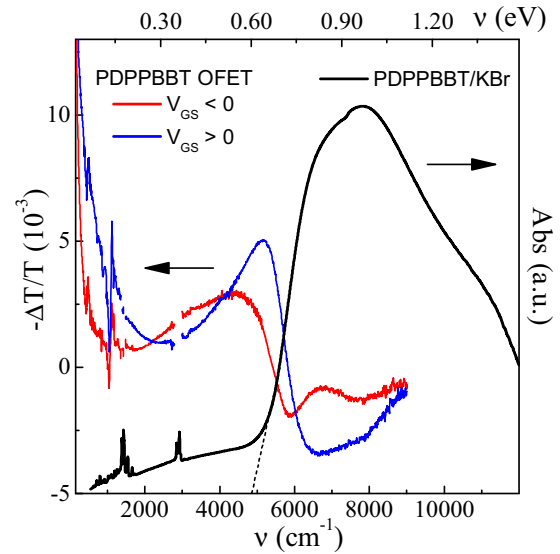


FIG. 4. (Color online) Left axis: broadband differential transmission spectra $\Delta T/T$ for a PDPPBBT OFET. Hole (electron) injection is denoted by the red (blue) curve. The very strong absorption at lower energies below 2000 cm^{-1} originates from the free carrier response in the Si substrate. Gaps in the spectra represent areas of strong absorption from the polypropylene cryostat windows. Right axis: absorption spectrum for thin-film PDPPBBT deposited on a KBr substrate. The dotted line intersecting the frequency axis indicates an estimate for the optical bandgap.

superimposed on a linear absorption spectrum for a thin film of PDPPBBT deposited on a KBr substrate (black curve).

The neutral polymer absorption in Fig. 4 reaches a maximum near 1 eV. The optical energy gap is typically obtained by linear extrapolation of the low-energy end of the primary absorption band [40]. Here we extracted an optical gap of 0.60 eV. We note that our estimated gap value is in agreement with previous absorbance and cyclic voltammetry measurements, where the electrochemical gap between the HOMO and LUMO levels was also estimated to be 0.65 eV [11].

It has been suggested that the lowest excited state in PDPPBBT is an intramolecular charge transfer (ICT) state, as opposed to a $\pi\text{-}\pi^*$ transition [41]. Previous density functional theory (DFT) calculations for BBT-based DA polymers predict a lowest-lying excited-state energy of 0.5 eV, providing a low onset of optical absorption [7]. Molecular orbital distributions show a HOMO that is delocalized across the entire DA molecule, while the LUMO is relatively localized on the donor, indicating some degree of intramolecular charge transfer during copolymerization [13,41]. The lowest-energy absorption band in absorbance spectra, however, has a larger oscillator strength than subsequent excited-state transitions, indicating that it is likely dominated by $\pi\text{-}\pi^*$ character [11]. Further, an ICT state or CT exciton would likely result in a large dipole moment. Under a strong applied electric field, a significant Stark shift would manifest in the spectra near the absorption edge, as seen previously in electroabsorption measurements [42–51]. We do observe some additional structure in the bleached absorption above the band edge in

Fig. 4. Electroabsorption measurements are typically fit to first- or second-derivative spectra to determine the origin of the band edge shifts. In charge modulation experiments, however, spectroscopic signatures of electroabsorption often show up as shoulders atop other electronic absorptions [24,52]. Given the smaller energy scale dictated by the midgap bound states and the polymer absorption edge, we cannot distinctly discriminate Stark-related features from the polaron or neutral absorption. We do note the lack of a significant temperature dependence on both the strength and structure of the field-induced excitations. Further, an extended discussion of the Stark effect is beyond the scope of this work.

We ascribe the field-induced subgap absorptions to the P_2^+ and P_1^- transitions for hole and electron polarons, respectively. The weaker bleaching of the neutral absorption near the bandgap under positive gate voltage is likely because some of the increase in transmission is offset by the high-energy tail of the electron polaron absorption occurring concurrently. The strength of the absorption decreases linearly with applied gate bias, shown in the top inset of Fig. 3.

We find a significant difference in absorption energies between electrons and holes in the IR spectra in Fig. 3. The electron polaron absorption (blue curve) has a peak energy of 3981 cm^{-1} , while the hole polaron (red curve) peak occurs at 3413 cm^{-1} . The difference in polaronic peak energies is interesting in that it reflects an intrinsic asymmetry in the electron and hole wave functions in the polymer structure. In DA polymers, the degree of ambipolarity is intimately tied to the constituent donor and acceptor moieties. As different molecules are substituted into the copolymer structure, the HOMO and LUMO energy levels can shift significantly, affecting the bandgap, environmental stability, and band offsets determining the charge injection properties for various metal contacts [2–7,11]. Electronic transport, especially, is extremely sensitive to the choice of donor. The emergence of high-mobility DA polymers with strong electron and hole transport is a result of both HOMO and LUMO electron orbitals that are often well delocalized over the entire DA molecule [6,7].

We can infer from the difference in peak energies that the electron polaron states are more weakly bound and lie slightly closer in energy to the extended states than the hole polarons. This is also reflected in the higher electronic mobility we observe in transistor characteristics in Fig. 2 and much higher drain current for a given gate voltage compared to that of holes. Our observations are consistent in general with the strong electron transport commonly observed in DPP-based copolymers. Slight shifts occur in the absorption peak energies for lower gate voltages, but these are much smaller than the energy difference between electron and hole polarons. Additionally, although plagued by a large background, the n -induced IRAVs appear to be much weaker than those for holes, also indicating a smaller degree of localization. Thus, with our spectroscopic probe we are afforded direct access to microscopic details of the electronic structure and fundamental differences in electron and hole behavior that are not available from transport measurements alone due to extrinsic effects (contact resistance, trapping, etc.).

To conclude this section, we comment on our previous studies investigating a similar class of small-bandgap polymers

based on BBT [25]. We found a remarkable symmetry in the IR spectra for both positive and negative gate voltages that we originally attributed to the existence of a self-doped polymer. We did not find significant absorption for positive gate voltages attributable to mobile electrons and thus concluded a hole-dominated polymer was responsible despite often showing balanced ambipolar OFET transport. We now understand the origin of this self-doping to be due to severe electron trapping, resulting in a highly hole-doped “off” state ($V_{GS} = 0\text{ V}$) to maintain electrostatic balance. The symmetry seen in the IR data is a result of enhancement/suppression of an existing hole polaron absorption in the unbiased polymer.

Our present work, where we observe distinct spectral features for both conducting electrons and holes, underscores the need for an extremely low pressure environment ($<10^{-5}\text{ mbar}$) afforded to us by using a high-vacuum cryostat. We were unable to reproduce gate-induced absorption data shown in Figs. 3 and 4 in our broadband FTIR spectrometer, where the ambient pressure is 2 mbar, without the use of a cryostat. Such a drastic dependence on ambient conditions indicates that charge trapping from water moisture and ambient air dominates the bias stress in these small-gap DA polymer devices, as well as trap states from the SiO_2 interface [24,30,53–56].

C. Infrared microscopy

Having established the spectral features associated with mobile electrons and holes in PDPPBBT, we employed IR microscopy to probe the charge injection landscape and dynamic response with $20\text{-}\mu\text{m}$ spatial resolution, much smaller than the OFET source-drain separation ($d = 200\text{ }\mu\text{m}$). For various voltage configurations, we expect very different carrier distributions in the transistor channel, especially during ambipolar operation when both negative and positive charges contribute to the current.

Figure 5(a) shows representative IR absorption microscopy spectra for the PDPPBBT device biased in the ambipolar regime, where $V_{GS} = +80\text{ V}$ and $V_{DS} = +120\text{ V}$, as a function of position. The format of Fig. 5(a) is a three-dimensional (3D) plot using a logarithmic color scale to indicate the strength of absorption, and a two-dimensional (2D) color-map projection of the IR spectra in the base plane as a visual aid. Starting from the source ($x = 0\text{ }\mu\text{m}$), we find strong electron polaron absorption at the charge injection point ($V_{GS} = +80\text{ V}$). As the lateral drain field is increased, charges flow from the source to drain, and the current increases. At the same time, however, the strength of the gate field also decreases as the drain is approached, where the potential is $V_{GD} = V_{GS} - V_{DS}$.

As x increases, we see a systematic decrease in the strength of the electron polaron absorption until an electrically neutral point of zero potential is reached close to the drain, near $x = 150\text{ }\mu\text{m}$. After this crossover point, the channel potential is now negative with respect to the gate, resulting in a negative electric field and an injection of holes. This is reflected by an increase in absorption due to the accumulation of mobile holes. At the end of the conduction channel, where the drain potential is $V_{GD} = -40\text{ V}$, we find a moderate hole polaron absorption.

Gray dotted lines in Fig. 5(a) mark the peak frequency positions of the electron and hole polaron absorptions extracted

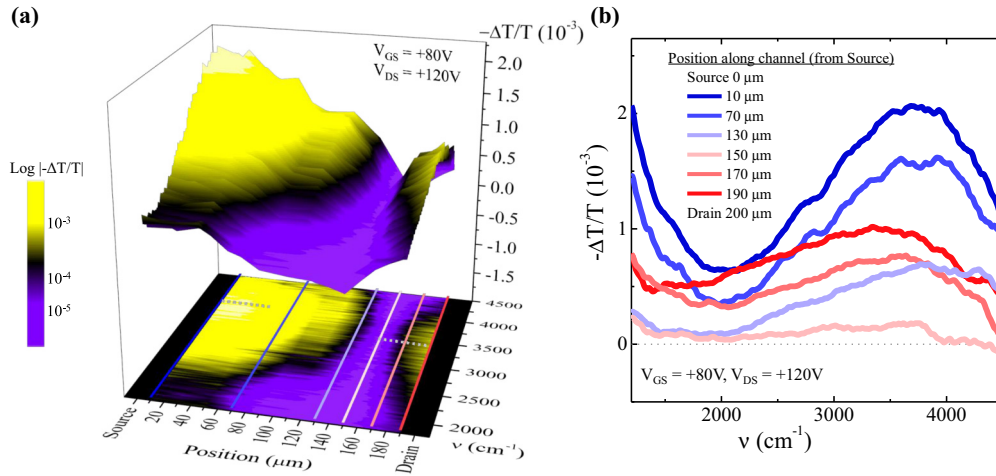


FIG. 5. (Color online) Representative IR microscopy data for a PDPPBBT device operating in the ambipolar regime with $V_{GS} = +80$ V and $V_{DS} = +120$ V. (a) 3D color plot visualizing the evolution of the polaronic absorption across the conduction channel. The IR beam size was reduced to $20 \mu\text{m}$ and scanned across the channel from the source electrode ($x = 0 \mu\text{m}$) to the drain ($x = 200 \mu\text{m}$). We find a prominent electron polaron absorption near the source gradually decreases in strength and eventually transitions to a weaker hole polaron absorption at the drain. A 2D color-map projection at the base of the graph shows the intensity of the IR response on a log scale, while colored lines indicate selected spectral slices. Gray dotted lines near the source and drain indicate peak frequency positions of electron and hole polarons, respectively. (b) Selected IR absorption curves for specific positions in (a), showing the clear distinction between electron (blue) and hole polarons (red).

from Fig. 3 ($\omega_e = 3981 \text{ cm}^{-1}$, $\omega_h = 3413 \text{ cm}^{-1}$). Figure 5(b) shows IR absorption curves representing selected spectral slices taken from the 3D plot in Fig. 5(a) (colored horizontal lines). The shaded color curves in Fig. 5(b) directly visualize the transition from electron polaron absorption (blue spectra) before the charge-neutral point near $x = 150 \mu\text{m}$ to hole polaron absorption (red spectra) as the drain at $x = 200 \mu\text{m}$ is approached. We do observe small shifts in polaron peak frequencies compared to the electrostatically doped device shown in Fig. 3; however, the distinction between electron and hole polarons is quite clear. We have repeated these experiments for other ambipolar biasing configurations, and the same charge-carrier-crossover behavior was observed, with polaron peak positions in general agreement with absorption spectra in Fig. 3.

From the strength of the polaron absorption, we can quantify the accumulation of mobile carriers in the transistor channel. Conventionally, the optical functions of a material are connected to the density of charges via the frequency sum rule [57]:

$$\int_0^\infty \frac{nc}{4\pi} \alpha(\nu) d\nu \propto \frac{N_e}{m_{\text{eff}}}. \quad (2)$$

We define a similar quantity N_{eff} proportional to the density of injected electrons or holes as

$$N_{\text{eff}} = \int_{\text{Pol}} -\frac{\Delta T}{T}(\nu) d\nu. \quad (3)$$

The differential spectra are integrated only over the broad polaron absorptions from 2000 to 5000 cm^{-1} .

Having established a quantitative measure of field-induced IR absorption, we connect the strength of this resonance directly to the number of charges, which can be independently

calculated either by assuming a simple capacitive model,

$$n_{2D} = \frac{\kappa \epsilon_0}{eL} V_{GS}, \quad (4)$$

or by measuring transient charging currents and thus calculating the total number of injected charges. The obtained doping-induced carrier density n_{2D} can then be correlated to the integrated intensity of the polaron absorption N_{eff} . We have previously shown this approach to be consistent with the linear capacitor model of an OFET [25,58].

We performed similar IR microscopy for four biasing regimes. Figure 6 shows a spatial map of the carrier density n_{2D} throughout the transistor channel, extracted from the totality of spectroscopic data for the respective gate and drain voltage configurations. The color of the shaded areas indicates the carrier type (red: holes, blue: electrons). For unipolar hole and electron operations [Figs. 6(a) and 6(b), respectively], we find a slow but steady suppression of the polaron absorption from the source to the drain electrode, where the charge density is pinched off.

During ambipolar device operation [Figs. 6(c) and 6(d)], there exist spatially separated hole-rich and electron-rich regions in the transistor channel, indicated by the red (hole) and blue (electron) shaded areas. The size of these regions, as well as the position of the electron-hole boundary, is determined by both the drain potential along the channel relative to the gate and the carrier threshold voltage V_{th} . On a microscopic level, the interface between electron- and hole-doped regions contains an area of carrier recombination with a finite width. Simulations and modeling of ambipolar transistors with Langevin recombination of holes and electrons predict the spatial extent of this region to be from hundreds of nanometers to several microns [59–61]. This recombination zone forms the basis for light-emitting field-effect transistors and has been experimentally measured for different polymer systems to be $\sim 2 \mu\text{m}$ [27,62–64]. The size of our

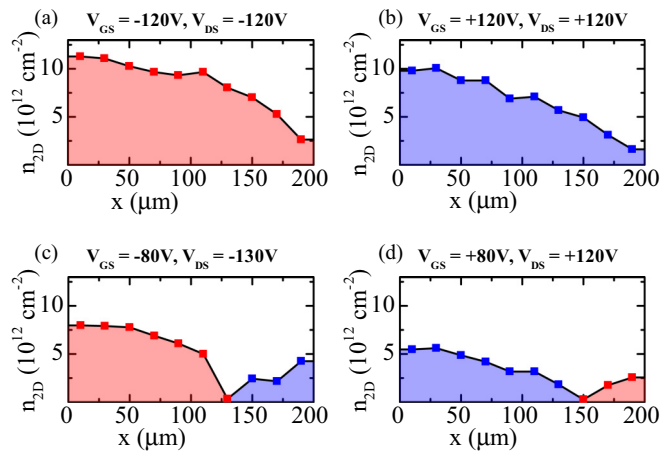


FIG. 6. (Color online) Charge density map across the conduction channel for (a) unipolar hole, (b) unipolar electron, and (c) and (d) ambipolar OFET device operation. Areas under the curve are filled with the color indicating the carrier type (red: holes, blue: electrons). The 2D charge density n_{2D} was extracted by comparing the integrated polaron absorption $N_{\text{eff}}^{\text{Pol}}$ at each location to that obtained from the electrostatically doped configuration in Fig. 3 and assuming linear device operation (top inset in Fig. 3), typically valid for SiO₂-based OFETs [25].

diffraction-limited beam, however, is on the order of the wavelength of IR light (10–15 μm). As a consequence, our IR beam will average over the recombination zone as well as small regions of weak electron and hole doping, resulting in an insignificant net change in the IR absorption, as seen in Fig. 5 at $x = 150 \mu\text{m}$. Thus, we cannot fully spatially resolve the recombination zone with IR microscopy alone, yet we are still able to directly observe the crossover from electron- to hole-induced excitations on a slightly larger length scale.

These data confirm the well-established notion that the charge density in the saturation regime of an OFET is highly nonuniform, which comes directly from the conventional equations for field-effect transistors [1]. However, very few studies have directly imaged this behavior using IR spectroscopy [56], and to our knowledge such spatio-spectral mapping has never been demonstrated for an ambipolar organic system in the IR range. Since the saturation regime is most often

invoked to estimate carrier mobility, a detailed account of the carrier distribution in the conduction channel, as well as the microscopic details provided by the spectroscopic features, is very useful for developing accurate models of OFET transport. This is especially important for ambipolar and light-emitting devices, where there is electron/hole coexistence in the transistor channel, as well as potentially important intrinsic differences between positive and negative charge carriers, as we have shown.

IV. SUMMARY

In summary, we have performed a systematic IR investigation of ambipolar charge injection in a small-bandgap DA copolymer PDPPBBT. We register distinct absorptions associated with negative and positive polarons and uncover an intrinsic electron/hole asymmetry in the electronic structure of the DA system. Using diffraction-limited IR microscopy, we explored the evolution of the polaronic absorptions along the conducting channel of a functional PDPPBBT OFET, biased in both unipolar and ambipolar operating modes. In the ambipolar regime, we observe a spatial transition from hole to electron polaron absorption, indicating the coexistence of both charge carriers in the transistor channel akin to a p - n junction diode [65]. Last, from the strength of the polaronic response, we constructed a spatial map of the charge carrier density from the source to the drain electrode in the various biasing regimes. Our microscopic IR beam directly probes, energetically and spatially, the electronic excited states and low-energy dynamics associated with charge injection in small-bandgap DA polymer systems. Thus, we have demonstrated that IR microscopy combined with electrical transport measurements provides a comprehensive experimental approach with access to important details of the electronic structure, as well as a real-space charge-density profile of functional transistor devices. This allows for a much more thorough and accurate characterization and modeling of transport behavior in organic semiconductors, especially ambipolar polymer systems.

ACKNOWLEDGMENTS

Work at UCSD is funded by DOE-BES Grant No. DE-FG02-00ER45799.

-
- [1] D. Braga and G. Horowitz, *Adv. Mater.* **21**, 1473 (2009).
- [2] C. J. DuBois, K. A. Abboud, and J. R. Reynolds, *J. Phys. Chem. B* **108**, 8550 (2004).
- [3] J. L. Brédas, *J. Chem. Phys.* **82**, 3808 (1985).
- [4] J. L. Brédas, A. J. Heeger, and F. Wudl, *J. Chem. Phys.* **85**, 4673 (1986).
- [5] Z. Chen, M. J. Lee, R. Shahid Ashraf, Y. Gu, S. Albert-Seifried, M. Meedom Nielsen, B. Schroeder, T. D. Anthopoulos, M. Heeney, I. McCulloch, and H. Sirringhaus, *Adv. Mater.* **24**, 647 (2012).
- [6] S. Cho, J. Lee, M. Tong, J. H. Seo, and C. Yang, *Adv. Funct. Mater.* **21**, 1910 (2011).
- [7] T. T. Steckler, X. Zhang, J. Hwang, R. Honeyager, S. Ohira, X.-H. Zhang, A. Grant, S. Ellinger, S. A. Odom, D. Sweat, D. B. Tanner, A. G. Rinzler, S. Barlow, J.-I. Bre, B. Kippelen, S. R. Marder, and J. R. Reynolds, *J. Am. Chem. Soc.* **131**, 2824 (2009).
- [8] E. Ahmed, S. Subramaniyan, and F. Kim, *Macromolecules* **44**, 7207 (2011).
- [9] J. D. Yuen, R. Kumar, D. Zakhidov, J. Seifert, B. Lim, A. J. Heeger, and F. Wudl, *Adv. Mater.* **23**, 3780 (2011).
- [10] X. Zhang, T. T. Steckler, R. R. Dasari, S. Ohira, W. J. Potscavage, S. P. Tiwari, S. Coppée, S. Ellinger, S. Barlow, J.-L. Brédas, B. Kippelen, J. R. Reynolds, and S. R. Marder, *J. Mater. Chem.* **20**, 123 (2010).

- [11] J. D. Yuen, J. Fan, J. Seifert, B. Lim, R. Hufschmid, A. J. Heeger, and F. Wudl, *J. Am. Chem. Soc.* **133**, 20799 (2011).
- [12] P. Sonar, S. P. Singh, Y. Li, M. S. Soh, and A. Dodabalapur, *Adv. Mater.* **22**, 5409 (2010).
- [13] J. Lee, S. Cho, J. H. Seo, P. Anant, J. Jacob, and C. Yang, *J. Mater. Chem.* **22**, 1504 (2012).
- [14] Y. Zhang, C. Kim, J. Lin, and T.-Q. Nguyen, *Adv. Funct. Mater.* **22**, 97 (2012).
- [15] T.-J. Ha, P. Sonar, B. Cobb, and A. Dodabalapur, *Org. Electron.* **13**, 136 (2012).
- [16] H. Sirringhaus, P. J. Brown, R. H. Friend, M. M. Nielsen, K. Bechgaard, and A. J. H. Spiering, *Nature (London)* **401**, 685 (1999).
- [17] P. J. Brown, H. Sirringhaus, M. Harrison, M. Shkunov, and R. H. Friend, *Phys. Rev. B* **63**, 125204 (2001).
- [18] Z. Bao and J. Locklin, *Organic Field-Effect Transistors* (Taylor and Francis, Boca Raton, FL, 2007).
- [19] R. Österbacka, C. P. An, X. M. Jiang, and Z. V. Vardeny, *Science* **287**, 839 (2000).
- [20] R. Tautz, E. Da Como, T. Limmer, J. Feldmann, H.-J. Egelhaaf, E. von Hauff, V. Lemaure, D. Beljonne, S. Yilmaz, I. Dumsch, S. Allard, and U. Scherf, *Nat. Commun.* **3**, 970 (2012).
- [21] A. Cravino, H. Neugebauer, S. Luzzati, M. Catellani, A. Petr, L. Dunsch, and N. S. Sariciftci, *J. Phys. Chem. B* **106**, 3583 (2002).
- [22] Z. Q. Li, G. M. Wang, N. Sai, D. Moses, M. C. Martin, M. Di Ventra, A. J. Heeger, and D. N. Basov, *Nano Lett.* **6**, 224 (2006).
- [23] N. Sai, Z. Q. Li, M. C. Martin, D. N. Basov, and M. Di Ventra, *Phys. Rev. B* **75**, 045307 (2007).
- [24] Z. Chen, M. Bird, V. Lemaure, G. Radtke, J. Cornil, M. Heeney, I. McCulloch, and H. Sirringhaus, *Phys. Rev. B* **84**, 115211 (2011).
- [25] O. Khatib, J. D. Yuen, J. Wilson, R. Kumar, M. Di Ventra, A. J. Heeger, and D. N. Basov, *Phys. Rev. B* **86**, 195109 (2012).
- [26] E. C. P. Smits, T. D. Anthopoulos, S. Setayesh, E. van Veenendaal, R. Coehoorn, P. W. M. Blom, B. de Boer, and D. M. de Leeuw, *Phys. Rev. B* **73**, 205316 (2006).
- [27] J. Zaumseil and H. Sirringhaus, *Chem. Rev.* **107**, 1296 (2007).
- [28] B. Lee, A. Wan, D. Mastrogianni, J. E. Anthony, E. Garfunkel, and V. Podzorov, *Phys. Rev. B* **82**, 085302 (2010).
- [29] R. Häusermann and B. Batlogg, *Appl. Phys. Lett.* **99**, 083303 (2011).
- [30] Y. Yan, Q.-J. Sun, X. Gao, P. Deng, Q. Zhang, and S.-D. Wang, *Appl. Phys. Lett.* **103**, 073303 (2013).
- [31] B. Horovitz, *Solid State Commun.* **41**, 729 (1982).
- [32] E. Ehrenfreund, Z. Vardeny, O. Brafman, and B. Horovitz, *Phys. Rev. B* **36**, 1535 (1987).
- [33] H. Neugebauer, *J. Electroanal. Chem.* **563**, 153 (2004).
- [34] X. M. Jiang and R. Österbacka, *Adv. Funct. Mater.* **12**, 587 (2002).
- [35] R. Österbacka, X. Jiang, C. An, B. Horovitz, and Z. Vardeny, *Phys. Rev. Lett.* **88**, 226401 (2002).
- [36] Y. H. Kim, D. Spiegel, S. Hotta, and A. J. Heeger, *Phys. Rev. B* **38**, 5490 (1988).
- [37] A. J. Heeger, S. Kivelson, J. Schrieffer, and W. Su, *Rev. Mod. Phys.* **60**, 781 (1988).
- [38] Y. H. Kim and A. J. Heeger, *Phys. Rev. B* **40**, 8393 (1989).
- [39] B. Horovitz, R. Österbacka, and Z. Vardeny, *Synth. Met.* **141**, 179 (2004).
- [40] J. Tauc and A. Menth, *J. Non-Cryst. Solids* **8**, 569 (1972).
- [41] Y. Li, J. Cui, J. Zhao, J. Liu, P. Song, and F. Ma, *Sci. World J.* **2013**, 890215 (2013).
- [42] G. Weiser, *Phys. Status Solidi A* **18**, 347 (1973).
- [43] I. H. Campbell, T. W. Hagler, D. L. Smith, and J. P. Ferraris, *Phys. Rev. Lett.* **76**, 1900 (1996).
- [44] A. Horvath, G. Weiser, G. L. Baker, and S. Etemad, *Phys. Rev. B* **51**, 2751 (1995).
- [45] L. Sebastian and G. Weiser, *Chem. Phys.* **62**, 447 (1981).
- [46] G. Weiser, *Phys. Rev. B* **45**, 14076 (1992).
- [47] D. Guo, S. Mazumdar, S. N. Dixit, F. Kajzar, F. Jarka, Y. Kawabe, and N. Peyghambarian, *Phys. Rev. B* **48**, 1433 (1993).
- [48] S. Al Jalali and G. Weiser, *J. Non-Cryst. Solids* **41**, 1 (1980).
- [49] G. Weiser, *J. Appl. Phys.* **43**, 5028 (1972).
- [50] F. Feller and A. P. Monkman, *Phys. Rev. B* **60**, 8111 (1999).
- [51] S. Haas, H. Matsui, and T. Hasegawa, *Phys. Rev. B* **82**, 161301 (2010).
- [52] M. J. Lee, Z. Chen, R. di Pietro, M. Heeney, and H. Sirringhaus, *Chem. Mater.* **25**, 2075 (2013).
- [53] R. Di Pietro, D. Fazzi, T. B. Kehoe, and H. Sirringhaus, *J. Am. Chem. Soc.* **134**, 14877 (2012).
- [54] R. Di Pietro and H. Sirringhaus, *Adv. Mater.* **24**, 3367 (2012).
- [55] A. Salleo, T. W. Chen, A. R. Völkel, Y. Wu, P. Liu, B. S. Ong, and R. A. Street, *Phys. Rev. B* **70**, 115311 (2004).
- [56] X. Y. Chin, J. Yin, Z. Wang, M. Caironi, and C. Soci, *Sci. Rep.* **4**, 3626 (2014).
- [57] F. Wooten, *Optical Properties of Solids* (Academic, New York, 1972).
- [58] O. Khatib, B. Lee, J. Yuen, Z. Q. Li, M. Di Ventra, A. J. Heeger, V. Podzorov, and D. N. Basov, *J. Appl. Phys.* **107**, 123702 (2010).
- [59] G. Paasch, Th. Lindner, C. Rost-Bietsch, S. Karg, W. Reiss, and S. Scheinert, *J. Appl. Phys.* **98**, 084505 (2005).
- [60] M. Kamerink, D. S. H. Charrier, E. C. P. Smits, S. G. J. Mathijssen, D. M. de Leeuw, and R. A. J. Janssen, *Appl. Phys. Lett.* **93**, 033312 (2008).
- [61] M. Muccini, W. Koopman, and S. Toffanin, *Laser Photonics Rev.* **6**, 258 (2012).
- [62] J. S. Swensen, J. D. Yuen, D. Gargas, S. K. Buratto, and A. J. Heeger, *J. Appl. Phys.* **102**, 013103 (2007).
- [63] J. Zaumseil, R. H. Friend, and H. Sirringhaus, *Nat. Mater.* **5**, 69 (2006).
- [64] S. Z. Bisri, C. Piliego, J. Gao, and M. A. Loi, *Adv. Mater.* **26**, 1176 (2014).
- [65] P. Stallinga and H. Gomes, *Synth. Met.* **156**, 1305 (2006).